Overview of the emissivity measurements performed in WEST: in-situ and post-mortem observations

J. Gaspar, Y. Corre, F. Rigollet, M.-H. Aumeunier, E. Bernard, S. Brezinsek, X. Courtois, R. Dejarnac, M. Diez, L. Dubus, et al.

Overview of the emissivity measurements performed in WEST: in-situ and post-mortem observations

J. Gaspar, Y. Corre[a], F. Rigollet, M-H. Aumeunier[a], E. Bernard[a], S. Brezinsek[b], X. Courtois[a], R. Dejarnac[c], M. Diez[a], L. Dubus[a], N. Ehret, N. Fedorczak[a], M. Firdaouss[a], M. Houry[a], M. Le Bohec[a], T. Loarer[a], C. Martin[d], V. Moncada[a], P. Moreau[a], C. Pocheau[a], P. Reilhac[a], E. Tsitrone[a] and the WEST team*

Aix Marseille Univ, CNRS, IUSTI, Marseille, France
[a] *CEA Cadarache, IRFM, F-13108 St Paul lez Durance, France*
[b] *Forschungszentrum Jülich, Institut für Energie- und Klimaforschung Plasmaphysik, 52425 Jülich, Germany*
[c] *Institute of Plasma Physics, The Czech Academy of Sciences, 182 00 Prague 8, Czech Republic*
[d] *Aix Marseille Univ, CNRS, PIIM, Marseille, France*
** See http://west.cea.fr/WESTteam*
Corresponding author email address: jonathan.gaspar@univ-amu.fr

Abstract. This paper summarizes the emissivity measurements performed on the plasma facing units (PFU) of the WEST lower divertor during the first phase of WEST running with a mix of actively cooled ITER-like PFUs made of bulk tungsten and inertially cooled PFUs made of graphite with a coating of tungsten. In-situ assessment of the emissivity and laboratory measurements after removing the W-coated graphite and ITER-grade PFUs from the WEST device are shown. The measurements exhibit a complex pattern with strong emissivity variation as function of space and time mainly explained with the variation of magnetic equilibrium (strike point location) as well as the plasma performances during the experimental campaigns. The exposed ITER-grade PFU exhibits sharp spatial variation of the emissivity from 0.05 to 0.85 at a monoblock scale (12mm) at the transition of the erosion (strike point location) and deposition (next to the strike point location) areas on the high field side. In the low field side, the emissivity varies from 0.12, at the strike point location, to 0.2 few cm away in the low field side direction. This emissivity range after exposure is much higher than the emissivity variation of unexposed PFU with emissivity from 0.09 to 0.15. In-situ observation performed on the W-coated graphite PFU shows a rapid evolution, typically few pulses, of the emissivity in the inner and outer strike point location. The whole spatial distribution is discussed as well as his variation due to the plasma operation from the start-up of WEST to the removal of the tungsten (W) coated graphite components.

1. Introduction

Infrared (IR) thermography is widely used in fusion research to study the heat load distribution on the plasma facing units (PFU) [1-3] as well as ensuring their protections [4-7]. To these ends, assessing the emissivity of tungsten (W) components, as used for the ITER divertor [8,9], is necessary to derive accurate surface temperature from radiation measured by infrared systems. The W emissivity is low and dependent on various parameters as wavelength, temperature, and surface state such as its composition (oxidation, impurities) and its structure (roughness, cracks, deposited layers). During plasma operation, the PFU surface state is expected to evolve as function of time because of the plasma wall interaction processes which are likely different from pulse to pulse. Consequently, this is strongly affecting the emissivity value and distribution [10-13]. As a first step, a dedicated setup has been developed to measure the emissivity of W samples representative of the WEST lower divertor, including samples with different damage levels generated by electron gun (micro-cracks and crack network) [14]. The experimental results show, as expected, the dependencies with wavelength, temperature and surface state (roughness, cracks, pollution by impurities). For the same wavelength and temperature, the surface state shows a strong influence with a large increase of the emissivity with the micro crack and cracks network, by a factor up to 4. However, the samples used in this study did not see plasma operation that

could have modified the surface state through plasma surface interaction (erosion, deposition and possible damages) [15-17]. As a second step, an in-situ method has been developed to assess the emissivity evolution of the WEST divertor PFUs [18]. The method is based on the measured infrared (IR) radiance, coming from isothermal PFUs at several temperature levels, to be compared with embedded thermal sensors before each pulse with the consideration of multiple reflection through photonic modelling. The third step relies on post-mortem measurements to carefully evaluate the emissivity in laboratory.

This paper presents an overview of the emissivity measurements performed on the WEST divertor PFUs of the first phase of WEST where the divertor is composed with a mixt of W-coated graphite and ITER-grade PFUs. The paper is divided in two parts, the first part shows the in-situ assessment of the W-coated graphite PFUs. The method developed in [18] has been applied over two experimental campaigns showing significant progress regarding the plasma performances (time duration and injected power). The emissivity distribution and its evolution with the plasma conditions: strike point location, cumulated time and energy, wall conditioning and fueling (H/D/He) are discussed. The entire W-coated graphite components have recently been removed to equip the lower divertor with actively cooled components (WEST phase 2) allowing post-mortem studies. The second part of the paper summarizes the post-mortem emissivity measurements performed in laboratory. The emissivities of W-coated and ITER-grade PFUs have been measured for a large number of PFUs allowing the observation of the emissivity distribution over a ripple modulation (toroidal section of 20° of the machine) but also within a millimeter scale.

2. Emissivity evolution during WEST operation

2.1. Thermal measurements and emissivity calculation

The phase 1 of operation of WEST extending from 2017 to 2020 is composed by five experimental campaigns named from C1 to C5 [19]. During this period, 3889 plasmas have been performed for a total plasma duration of about 7h15 and 21.2 GJ of cumulated injected energy, mainly electron heating using lower hybrid launchers (LHCD heating), in various divertor configurations: lower single null (LSN), upper single null (USN) and double null (DN). In LSN configuration the inner strike point (ISP) and outer strike point (OSP) are located on the lower divertor which is composed by 12 independent toroidal sectors of 30°. Each sector is equipped by 38 plasma facing units (PFUs), thus a total of 456 PFUs is required to cover the full divertor ring (see figure 1 a). During the phase 1, the lower divertor was composed of a mix of actively cooled ITER-like and inertially cooled W-coated graphite PFUs. A set of ITER-grade PFUs based on the W monoblock concept with 35 flat monoblocks (MB) of individual size ~28 mm × 12 mm × 26 mm (width × depth × height) assembled with a gap of 0.5 mm on a CuCrZr heat sink tube [20] have been tested before the full completion of the divertor foreseen in phase 2. The number of ITER-grade PFU increased over the campaigns with 6 PFUs during C1 and C2, 12 PFUs during C3 and 14 PFUs during C4. The lower divertor was completed with inertially cooled graphite PFUs with a W-coating (~15 µm) and 1° toroidal bevel geometry, each unit is composed by one component for the ISP (high field side) and one for the OSP (low field side [21] (see figure 1b)).

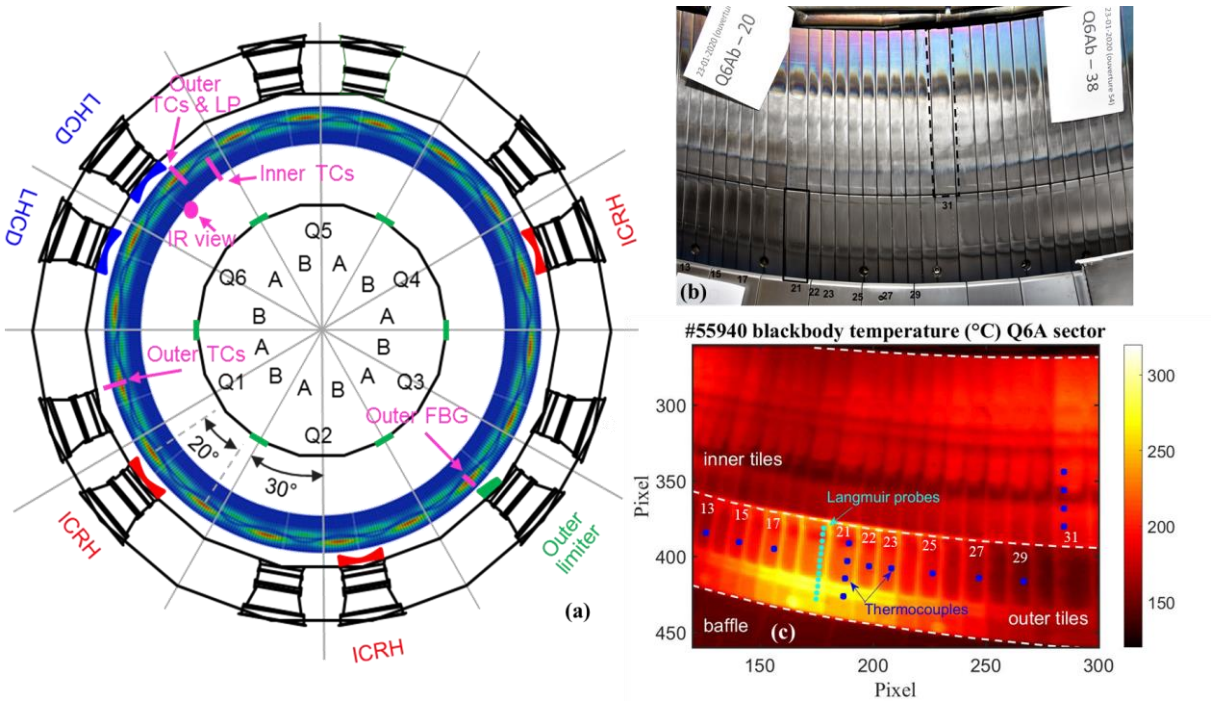

Figure 1. (a) Top view of the machine with typical heat load pattern on the lower divertor due to the ripple modulation (20°), the sector distribution, the Ion Cyclotron Resonance Heating (ICRH) and Lower Hydrid Current Drive (LHCD) antennas and diagnostics. (b) Picture of the sector Q6A after the 2019 campaign (C4). A total of 10 W-coated graphite PFUs were equipped with 16 TCs which are indicated by their tile number on (b) and (c). In this section, we investigate TC measurements located on the outer #21 and inner #31 tiles. (c) Blackbody temperature measured by the IR view before the pulse starts (featuring homogenous tile temperatures) with the tile numbers and the diagnostics location.

The temperature of the WEST lower divertor is monitored during and in-between pulses by a set of complementary thermal diagnostics: 20 thermocouples (TCs) sensors embedded in the component at 7.5mm below the surface [22], 4 Fiber Bragg Grating (FBG) probes including 11 sensors each [23] embedded at 3.5 and 7mm below the surface and standard IR thermography systems [4]. The standard IR system used in this analysis consists of actively cooled endoscope located at the top of the chamber monitoring the lower divertor. The IR cameras are equipped with a narrow filter at the wavelength 3.9 ± 0.1µm with a frame size of 640x512 pixels. The IR system is calibrated and translate the collected radiance into blackbody surface temperature (emissivity equal to 1). The projected pixel size is about 2.5 mm/pixel for the reported PFU studied in this paper. One IR camera is monitoring a sector (Q6A) equipped with onboard diagnostics 16 TCs including broader PFUs with 4 TCs (x2 inner and outer) and flush-mounted LPs [24] as illustrated in fig 1 c). These PFUs are located at the maximal heat load location due to the ripple magnetic field modulation (PFU#21 for the outer and PFU#31 for the inner side respectively). The following analysis is based on this two PFUs for the in-situ measurements. The last 4 TCs are installed in another sector not studied here.

The temperature of the inertial W-coated graphite PFUs increases over the day due to the repetition of energetic pulses while the rest of the vacuum vessel is maintained at 70°C thanks to the water cooling loops. During the C4 campaign from July to November 2019, 1442 discharges have been performed, in which 1112 and 330 are fueled with deuterium and helium respectively, corresponding to a cumulated plasma duration of 9678 s and 2991 s. The total injected energy (radio frequency and inductive heating) is about 15.96 GJ with almost 6.31 GJ conducted to the divertor for a duration of 10112 s in LSN configuration. For the C4 campaign, about 20 days exhibit divertor temperature increase sufficiently high to estimate the emissivity. Figure 2 a) shows the evolution of the initial temperature (as recorded

before the pulses with the TC system) over the last 4 days of the campaign (helium campaign) with an initial temperature increase from 70°C up to 345°C and 246°C for OSP (red) and ISP (blue) PFUs, respectively. The rest of the device is mainly kept to 70°C the temperature of the water-cooling loop. The figure 2 b) shows the toroidal distribution of the initial temperature for the 10 instrumented PFUs that follows the ripple modulation.

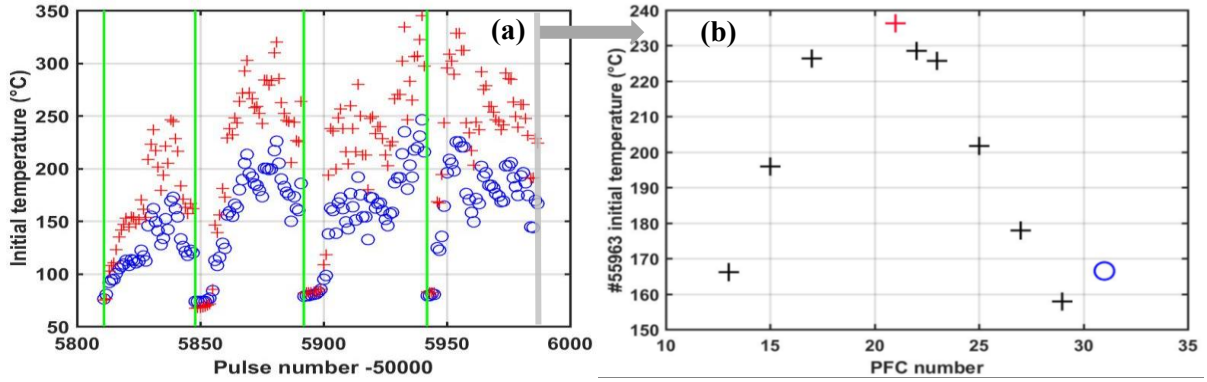

Figure 2. (a) Evolution of the initial temperature over the last 4 days of the C4 campaign, helium plasma, for OSP PFU #21 (red cross) and ISP PFU #31 (blue circle) PFUs. The green vertical lines correspond to the first pulse of each day. (b) Toroidal distribution of the initial temperature for the pulse #55987 for the 10 instrumented PFUs (red cross) PFU #21, (blue circle) PFU #31 and (black cross) PFU #13 to #29.

In [18] a method was developed to estimate in-situ the emissivity of the W-coated graphite divertor tiles in the WEST tokamak. The method is based on the simultaneous recording of the IR radiance and TC coming from isothermal PFU at several temperature levels before each pulse. The collected radiance is composed of two terms. The first one is the emitted radiance depending on PFUs temperature and its emissivity, the second one is the reflected radiance coming from the surrounding and self-reflection of the divertor on itself due to multiple reflection in the metallic high reflective environment. The radiance is measured twice, when the PFU is at the two different temperatures T_1 and T_2. The measured radiances by the IR system can be written as follows:

$$L_{m1} = \varepsilon L_{BB1} + L_{r1} \quad (1)$$

$$L_{m2} = \varepsilon L_{BB2} + L_{r2} \quad (2)$$

where ε is the emissivity (supposed unchanged or low variation at the two temperatures), L_{m1} and L_{m2} are the measured radiances at the PFU temperatures T_1 and T_2, L_{BB1} and L_{BB2} are the blackbody radiances computed with the temperatures T_1 and T_2 given by the TCs, L_{r1} and L_{r2} are the reflected radiances when the PFU temperatures are at T_1 and T_2. Usually, L_{r1} and L_{r2} are considered equal. In the WEST tokamak environment, this assumption cannot be made due to the high reflective environment provided by metallic surfaces. In this configuration the reflected radiances variation must be calculated. The emissivity map is finally given by:

$$\varepsilon = \frac{(L_{m1} - L_{m2}) - (L_{r1} - L_{r2})}{(L_{BB1} - L_{BB2})} \quad (3)$$

Photonic simulations have been performed using the Monte Carlo raytracing code SPEOS CAAV5 [25] to calculate the variation of reflected radiance $\Delta L_r = L_{r1} - L_{r2}$ [18].

2.2. Evolution of the emissivity distribution along the divertor during C4

To follow the emissivity evolution during the C4 campaign, 160 pairs of pulses have been investigated from the pulse #54800 to #55987 coming from 20 different experimental days featuring significant temperature increase of the divertor. The pulses have been paired up with pulses of the same day to limit the emissivity variation between the two measurements. The selected pulses also fulfil the requirements on the TC measurement of $T_{init} > 95°C$ and heating between pulses higher than 30°C to have enough IR signal.

Figure 3 shows the emissivity map evolution for 7 pulses covering the C4 experimental campaign for the ISP tile #31 (top) and OSP tile #21 at the maximal heat flux location (therefore not at the same toroidal location as displayed in fig 1a). All the pulses are equivalent deuterium plasmas in terms of plasma current, density and injected power except for the last pulse which the last one of the helium campaign. For the deuterium plasmas the main difference for the 6 pulses is the magnetic equilibrium and especially the location of the outer strike point. The emissivity pattern exhibits sharp variations with poloidal and toroidal distribution, completely different on the ISP and OSP. The emissivity is found to be higher on the ISP than OSP, up to 0.6 on larger extend. On the ISP the high emissivity area also varies in the poloidal direction. On the OSP the low emissivity area is dominant and consistent with the outer strike point area featuring intensive sputtering processes over about few cm length (equivalent to the particle and heat flux decay length). The emissivity values displayed here are very close to emissivity measurement performed on pristine W coating 0.122 ± 0.006 [14] with the same wavelength (3.9µm) at 200°C. Still on the OSP, the area of high emissivity corresponds to the start of the magnetic shadowing induced by the baffle located above the lower divertor. One can also note the complex and discontinues evolution of the emissivity pattern along the C4 experimental campaign.

Figure 4 (a) shows the emissivity distribution evolution during C4 from the pulse #54811 to #55987 with color variation from blue to red. The emissivity distribution is extracted in the PFU center regarding the toroidal coordinate. Figure 4 (b) shows the cumulated conducted energy to the lower divertor as function of the strike point location computed with the magnetic reconstruction (EQUINOX [27]). The conducted energy is calculated as function of time, with the radiated power taken from the bolometry system and subtracted to the total injected power integrated with 0.5 s time step and distributed with 1/4 ISP and 3/4 OSP on each strike point location during this time step (to be consistent with the IN/OUT asymmetry reported in [26]). It is important to stress that the conducted energy plotted here have no consideration on heat flux decay length and the spatial resolution of the figure corresponds to the IR spatial resolution on these PFUs. One can note that the maximum cumulated energy is located between r=2.11 m and 2.15 m (corresponding to MB15-18) and r=2.21 m and 2.28 m (MB 25-26) for ISP and OSP respectively. The figures 3 and 4 illustrate the large variation of the emissivity during C4, especially on the inner side. The variations go from 0.12 ± 0.01, close to the pristine W-coating value, to 0.65 ± 0.05 showing a variation higher than a factor 5 for a single PFU that can be linked to an important variation of the surface state or structure as we can observe in the figure 1 b). It is important to stress that this variation (factor 5) is much higher than the emissivity variation due to temperature measured equal to 0.122 at 200°C and 0.148 at 550 °C as observed in laboratory [14].

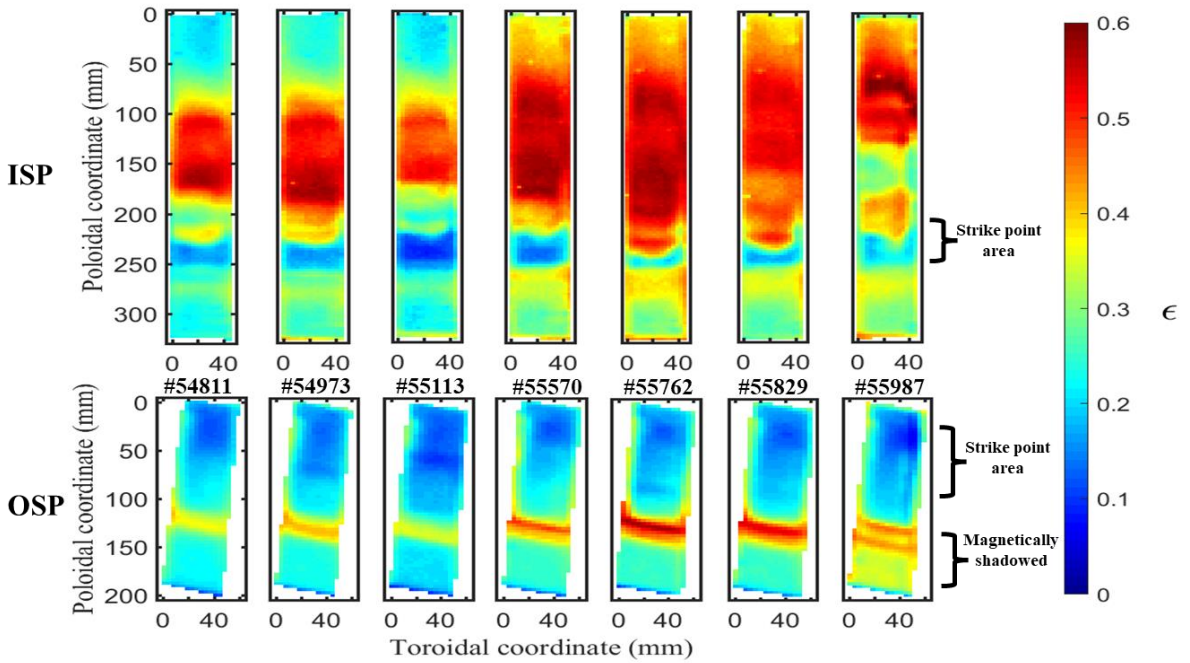

Figure 3. Emissivity map for the ISP tile #31 (top) and OSP tile #21 (bottom) of the sector Q6A during C4 for the pulses: #54811, #54973, #55113, #55570, #55762, #55829, #55987 (C4 end).

The emissivity distribution can be linked to pulse scenario and plasma parameters. In the figure 4 from the inner to the outer sides, the first arrow shows the increase of the emissivity from ~0.2 to ~0.5 constantly during C4 probably due to impurity accumulation 15 cm away from the inner strike point location, which is mainly at R = 2.13 m. The second arrow shows a strong decrease of the emissivity for 2.02 < R < 2.08 m from ~0.6 to ~0.4. This decrease happens during the last 4 days of C4 dedicated to helium plasmas, performed for PFU ageing study with the usual magnetic configuration (B_T = 3.7 T, X-point height about 75 mm) but with plasma current (Ip) equal to 300 kA contrary to deuterium plasma mainly performed with Ip = 500 kA. These two main differences could strongly affect the erosion re-deposition pattern in the inner side and explain the strong emissivity decrease probably by impurity removing in this area. The third location in the circle corresponds to an emissivity decrease at R=2.03 m for the last 13 helium plasmas performed with Ip=350 kA showing the sensitivity of the emissivity distribution to the plasma current. The fourth set of arrows illustrates the three principal outer strike point locations performed during C4. These locations can be also correlated to the locations where the emissivity is minimal at different moment in the campaign. These variations will be discussed in the next section.

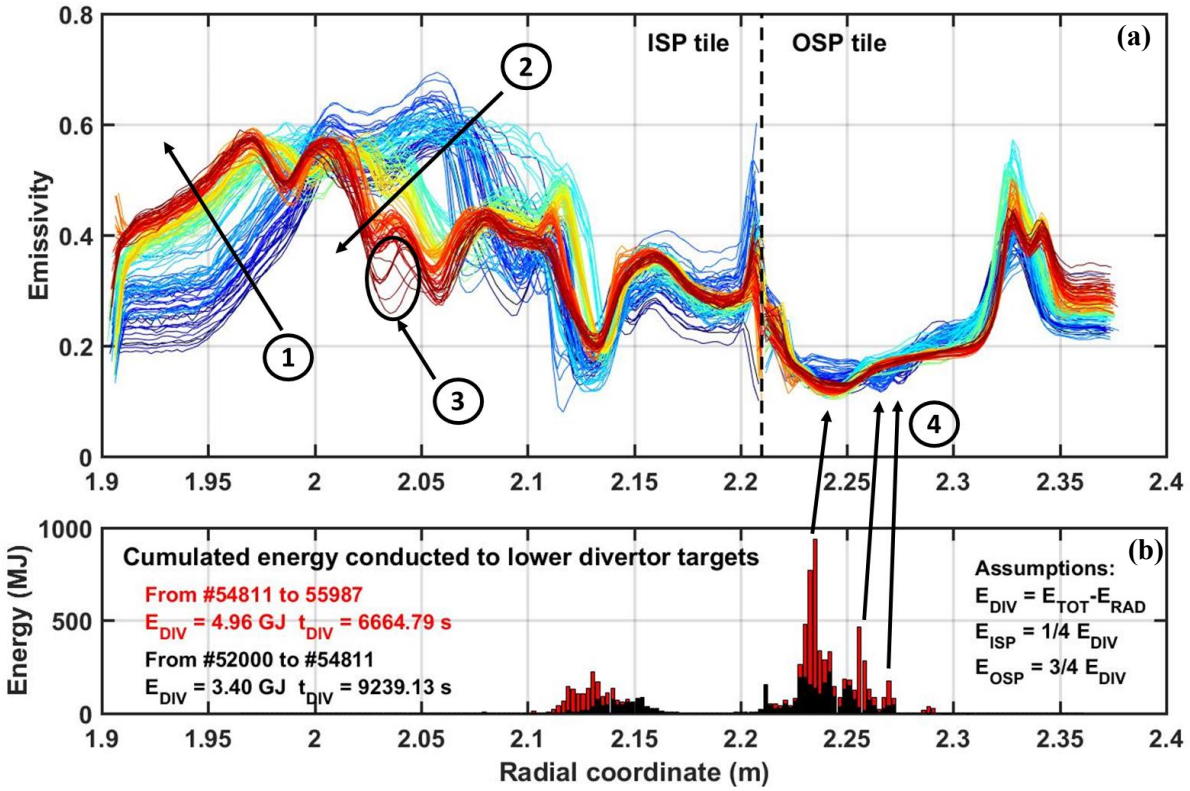

Figure 4. (a) Emissivity distribution along the lower divertor, for the ISP tile #31 and OSP tiles #21 of the sector Q6A, for 160 pair of pulses during the C4 campaign from the pulse #54811 (blue) to the pulse #55987 (red), with color graduation from blue to red. (b) Illustration of the conducted energy to the lower divertor at the strike point location with asymmetry of 1/4 ISP and 3/4 OSP as observed in [26] and no consideration of decay length (λ_q). (black) Conducted energy before the pulse #54811 and (red) between the pulses #54811 and #55987. (see Movie01 online)

2.3. Pulse to pulse emissivity variation near the outer strike point location:

During the C4 campaign, experiments have been performed with different X-point heights resulting in different outer strike point locations (from R=2.21 up to 2.29 m corresponding to MB24-28). Figure 5 shows the emissivity and conducted energy during 4 pulse sequences featuring fixed magnetic equilibrium (a, b, c and d) right after a change of strike point location. Emissivity and cumulated conducted energy before and after the pulse sequence (last pulse) are plotted in black and red respectively. The conducted energies for these pulses are: (a) 230 MJ for 12 similar pulses at R=2.27 m, (b) 720 MJ for 24 pulses at R=2.25 m, (c) 112 MJ for 8 pulses at R=2.29 m and (d) 2197 MJ for 106 pulses at R=2.235 m. These different periods correspond to experiment performed in the EU framework during C4 (a) PFU shaping experiment [28], (b) predamaged PFU experiment [29], (c) sustained melting experiment [30] and (d) the helium campaign [31]. The experiments (a), (b) and (c) have been performed with deuterium fueling and about 4 MW of LHCD heating, average core density was about 3.5 10^{19} m^{-3} and Ip = 500 kA. The main difference between the 3 sequences is the X-point height varying from 75 to 120 mm resulting in 3 different strike point locations. The pulse parameters of the helium campaign (d) are Ip=300-350 kA, average core density about 3.8 10^{19} m^{-3} and $P_{LH} \sim 4$ MW. The figure 5 shows the emissivity variation from 0.12 to 0.2 in few cm, equivalent to the heat flux decay length on the target. The comparison of the 4 selected experiments shows the correlation between the strike point location and the minimal emissivity location with an outer shift about 1 cm. The shift is inside the magnetic reconstruction uncertainty and coherent with the shift of few mm between strike point and maximal heat

flux location due to the power spreading in the private flux region. Sequences(a), (b) and (c) show that a fast emissivity modification after only few hundreds of second of cumulated plasma duration. Case (c) even shows a 20% decrease of the emissivity at R = 2.295 m for only 8 pulses with a conducted energy of 112 MJ. On the other side, the sequence (d) shows a stagnation for the emissivity profile when the same plasma scenario is repeated even for a long period of time (about 2000s), here 106 pulses with a conducted energy of 2197 MJ contrary to the inner side where the emissivity continues to vary as shown in the figure 4. The minimal emissivity value seems to converge to the value of the pristine W coating about 0.12, consistently with the assumption of net erosion area and therefore a surface structure mainly composed of tungsten atoms. The figure 5 (d) shows also that the hollow freshly made during the period (c), at R = 2.295 m, disappears and exhibits a more uniform emissivity profile in this area consistently with the particle and heat flux decay lengths. The emissivity pattern obtained during sequence (d) is the result of two major changes: the magnetic equilibrium and plasma wall interaction processes with helium plasma, combined with a potential effect of boronization performed between these two sequences. The boronization and glow discharge effects will be discussed in the next section.

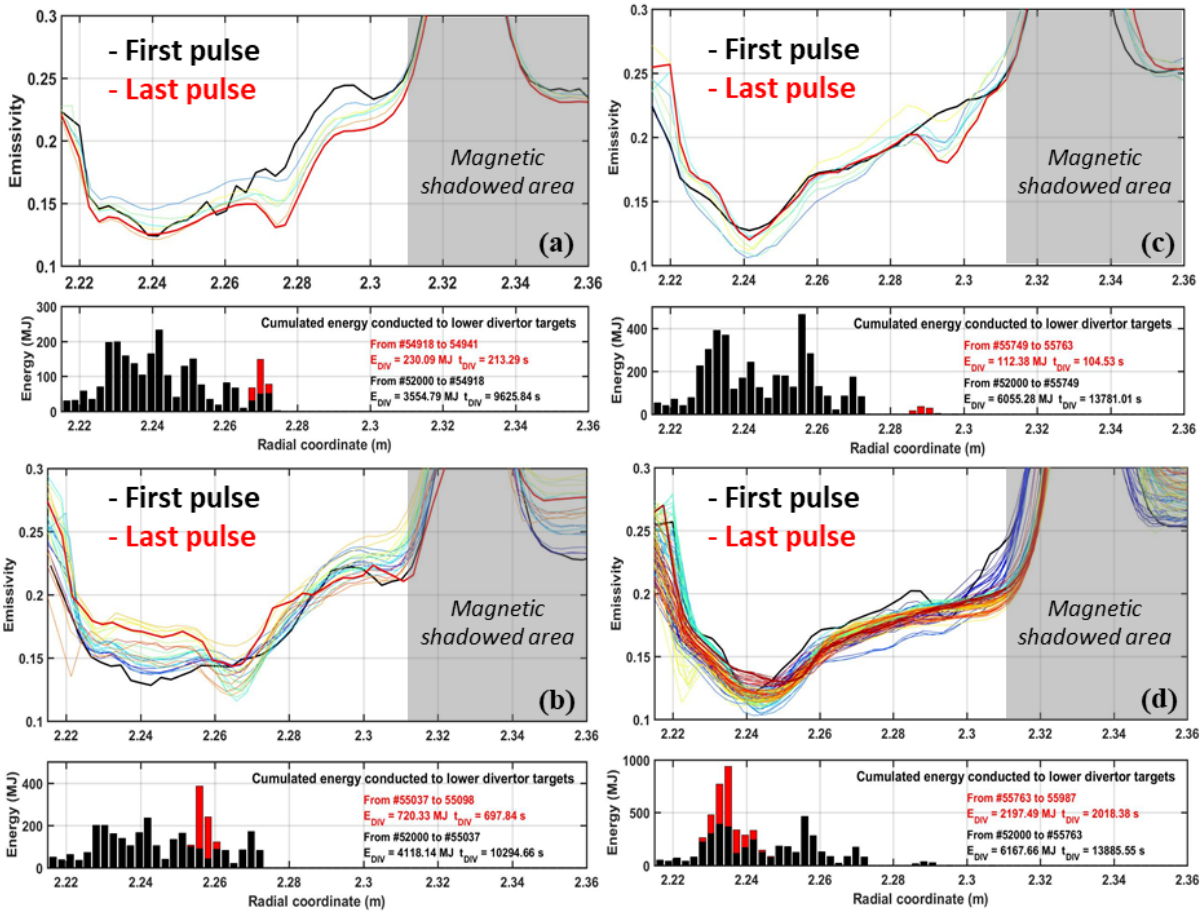

Figure 5. Emissivity distribution and conducted energy along the Q6A OSP tile #21 of the divertor for 4 experiments with different strike point location. Mean strike point location at: (a) R=2.27 m, (b) R=2.255 m, (c) R=2.29 m and (d) R=2.235 m. (black) Emissivity and conducted energy before the first pulse of the experiments and (red) emissivity for the last pulse and conducted energy over the experiment. (see Movie02 a/b/c/d online)

Figure 6 shows the emissivity distribution evolution during the predamaged PFU experiment (fig 5 b)) and the Langmuir probe measurements for the pulse #55070. The emissivity decrease is mainly in

the area where Te > 20 eV and ne > 2 10^{19} m^{-3}, leading to parallel heat flux > 40 $MW.m^{-2}$ and deposited heat flux about 3 $MW.m^{-2}$ on the beveled W-graphite PFUs.

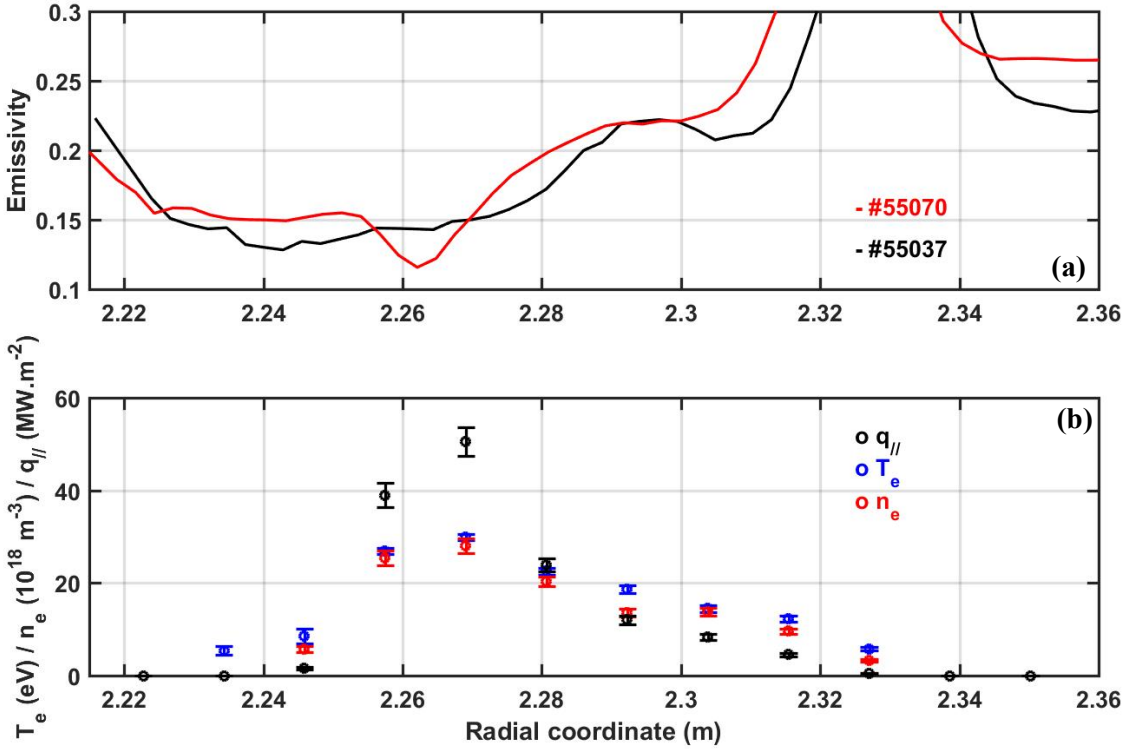

Figure 6. (a) Emissivity distribution along the Q6A OSP tile #21 of the divertor with strike point location at R=2.255 m, (black) first pulse of the experiment, (red) typical pulse of the experiment. (b) Langmuir probe measurement for the pulse #55070, (red) electron density, (blue) electron temperature and (black) parallel heat flux estimated assuming T_e=T_i ($q_{//} = \gamma J_{SAT} T_e$ with γ=7).

2.4. Effect of wall conditioning on emissivity

Wall conditioning is essential in fusion machine to achieve high plasma performance and reliable operational domain. The three conditioning techniques used in WEST is baking up to 200°C, glow discharge conditioning (GDC) [32] using deuterium or helium and boron wall coating through GDC of diborane called boronization. Baking is generally performed before the campaign begin. Deuterium or helium GDC are performed all along the campaign several times per week depending on wall condition and start-up performances. During C4 a total of 210 h with 160 h and 40 h of deuterium and helium GDC have been performed, respectively. Boronization have been performed 13 times during C4 for a total duration of 52 h of diborane GDC. The standard procedure of boronization starts with a deuterium GDC (1 to 4 hours), followed by a helium GDC (30min to 1 hour), then the diborane GDC begins and takes about 2 to 6 hours, depending on the diborane consumption rate. The last step is composed by again a helium GDC (about 40min) and sometimes deuterium GDC (1 to 3 hours). After boronization the surfaces are covered by a boron layer and the impurity flux released from the wall is reduced temporarily. The layer is eroded by the plasma, in particular near the strike point locations, and lose progressively his capability of reducing the impurity influx particularly for the oxygen [19]. As boron layer will cover the PFU after a bozonization, it is interesting to track the possible modification of the lower divertor emissivity after a boronization.

The 15th and 17th of October 2019 two consecutive boronizations have been performed because of an air leak happened the 16th of October with a vacuum vessel pressure increase from about 10^{-5} to 2.10^{-2} Pa. The air leak from a visible camera window was fixed after several hours and followed by deuterium GDC before the second boronization. The total duration of different GDC during this period is 10 hours of deuterium GDC, 3 h 30 min of helium GDC and 15 h 30 min of diborane GDC. Figure 7 shows the estimated emissivity of the last pulse (black) before the boronizations and the estimated emissivity three pulses (red) after it. The pulses used to get the emissivity are twins, they have the same magnetic configuration and cumulated energy of about 40 MJ. No strong modification of emissivity is seen except a 30 % increase at R= 2.09 m suggesting an accumulation on bore in this area (3 cm away from the inner strike point). On the outer side, the emissivity profiles are very close before and after boronization. Unfortunately, the emissivity cannot be estimated right after the boronization due to the need of divertor heating to perform the measurement. Nevertheless, we can conclude that the emissivity in the divertor is weakly affected by the boronization after few pulses.

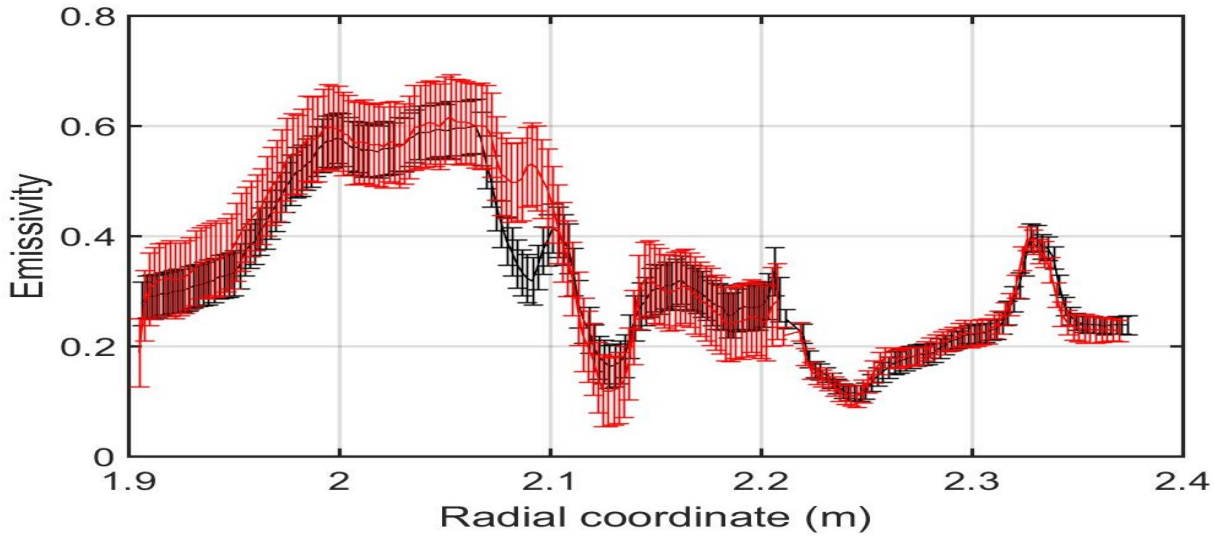

Figure 7. Emissivity distribution (black) before boronization and (red) three pulses after it, pulses #55541 and #55553, respectively.

2.5. Emissivity distribution before and after C5

Figure 8 shows the emissivity distribution along the divertor in the PFU center obtained with in-situ method at the end of C4 after the helium campaign [31] (black) and C5 after deuterium campaign(red) with the cumulated energy conducted to the divertor before and during C5. Post-mortem measurement performed in laboratory with the same filter ($3.9 \pm 0.1\mu m$) is also shown in the figure in blue. The testbed will be briefly described in the next section. The error bars correspond to the evaluated uncertainty due to the TC and IR measurements, here the uncertainty remains mainly on the IR measurement due to the low signal of the IR signal due to the narrow filter. First, the comparison of the emissivity distribution after C4 and C5 shows equivalent patterns, with a small increase of emissivity during C5 at the strike point areas and ~5 to ~10 cm away from the inner strike point area (R_{ISP}~2.13m) for ~2.02<R<~2.08m. Finally, the comparison of the in-situ assessment of the emissivity at the end of C5 (red) and the post-mortem measurement (blue) shows equivalent pattern but important discrepancies in the amplitude. The post-mortem measurement exhibits higher emissivity on most of the PFUs. Only the high field side edge (R<2m) of the inner PFU and the low field side edge (R>2.35m) show equivalent emissivities with the in-situ measurements. The difference is ~0.06 at the inner and outer strike point where the in-situ

assessment shows 0.13 ± 0.06 and 0.08 ± 0.03, respectively. This difference goes up to ~0.21 in the high emissivity areas where the emissivity is about 0.57 ± 0.08 (+37%) for the inner PFU and 0.35 ± 0.04 (+60%) for the outer PFU. Surprisingly the high emissivity area where the IR signal is higher are not the area with the best match. The post-mortem measurement has been performed 9 months after the end of C5 with the machine put back to the atmosphere, handling to remove the PFUs from the machine, storage under atmosphere and packaging to the laboratory. These several steps could modify the surface state of the PFUs leading to a variation especially in the high emissivity area where the impurity deposition is maximal. The differences could also come from the complementary sources regarding the IR emission and collection. First, a degradation of the IR transmission could lead to error on the in-situ assessment as the method relies on the IR calibration with a constant transmission during the campaign. But measurement of the optics after C5 reveals no significant change on the transmission of the IR systems during this campaign. Secondly, the in-situ emissivity calculated with the equation 3 uses a correction factor due to the evolution of the reflected radiance in the two thermal scenes used for the calculation. This reflected radiance variations have been evaluated with the photonic code SPEOS with simplified assumption as uniform low emissivity of the divertor. The consideration of non-uniform emissivity with high emissivity on the divertor could lead to a decrease of this correction. However, this correction of ~10% [18] is lower than the emissivity differences observed which is from 37 to 60% for the high and low emissivity area, respectively. Work is ongoing to disentangle the contribution of the different points. For the last point, work is ongoing to develop an inverse method based on the numerical twin of the WEST tokamak to estimate the emissivity distribution instead of using the double heating method [33] without assumption on their values or distribution.

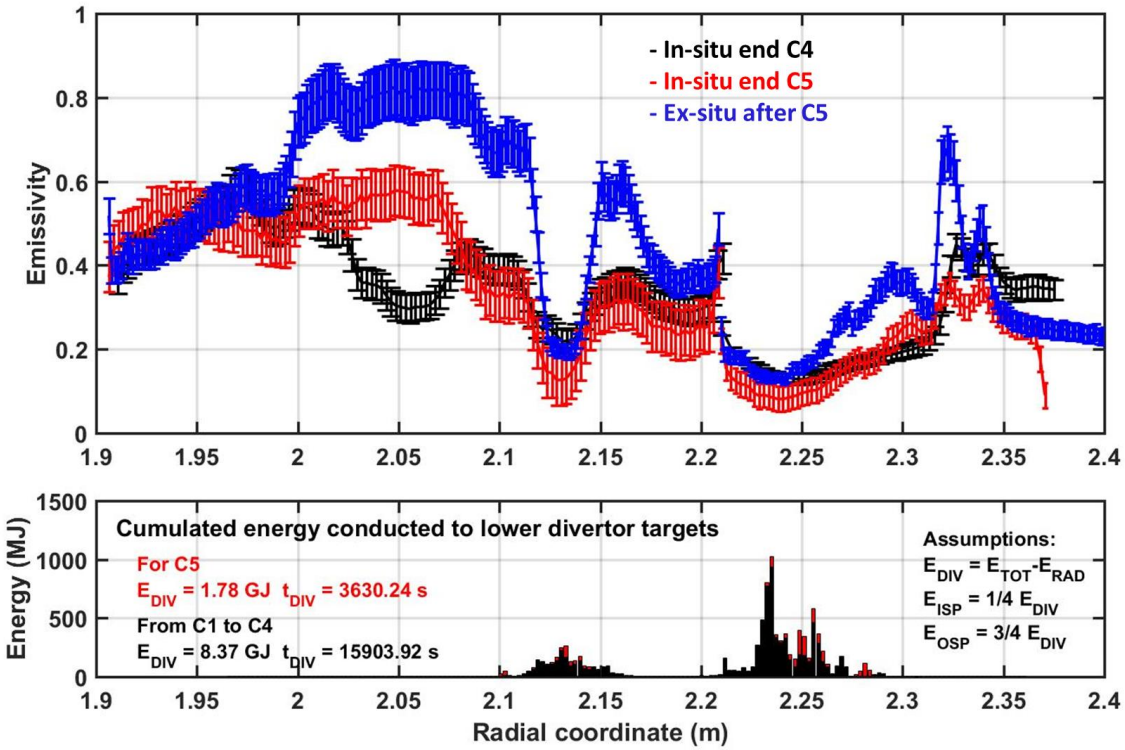

Figure 8. (a) Emissivity distribution along the lower divertor, for the ISP tile #31 and OSP tile #21 of the sector Q6A, for (black) the last pulse of C4, (red) the last pulse of C5 and (blue) ex-situ measurement after C5. (b) Illustration of the conducted energy to the lower divertor at the strike point location with asymmetry of 1/4 ISP and 3/4 OSP as observed in [26] and no consideration of heat flux decay length (λ_q). (black) Conducted energy from (black) C1 to C4 and (red) for C5.

3. Post-mortem emissivity measurement after the WEST phase 1

During the shutdown between C4 and C5 the W-coated PFUs and the unshaped ITER-grade PFUs of the sectors Q4B and Q3B, see figure 9 a) and c), have been replaced by ITER-like PFUs with toroidal bevel of 1° as expected in ITER. From the 76 PFUs only the PFU#18 of the Q3B sector has been kept for C5 and installed at the location #8, where heat load is maximum due to the ripple modulation, in order to perform melting experiment on the monoblock #28 [30]. To complete the in-situ observations, the emissivity of the removed PFUs have been measured in laboratory, especially for the ITER-grade PFUs for which the emissivity cannot be monitored in the machine because they are actively cooled.

Two dedicated testbeds have been developed to measure the emissivity map of the full actively cooled and W-coated graphite PFUs. The double heating method is used to obtain the emissivity using the equation 3. As we control the testbed environments, we can consider here L_{r1}=L_{r2} at the two temperatures, simplifying the emissivity calculation and reducing potential errors on the evaluation of the reflected flux evolution. For the ITER-like PFU testbed, the PFUs are heated though the PFU cooling tube using thermostatic bath. While for the second testbed, the W-coated graphite PFUs are heated in an oven. In both testbeds the PFUs are heated at 30°C and 70°C, each temperature the PFUs are measured by an IR camera in the wavelength range from 3 to 5 µm, contrary to 3.9 ± 0.1 µm in the machine, to optimize the signal noise ratio at this temperature level. The frame size is of 640x512 pixels, a 25 mm lens is used to get the full PFUs with a projected pixel about 0.7mm/pixel. A 50 mm lens with an extension ring is also used to have a field of view of about 4 monoblocks of the ITER-like PFU with a projected pixel about 0.08mm/pixel close to the very high-resolution IR view [1]. The uncertainty on the measured emissivities is about 4% and has been evaluated with Monte Carlo error propagation calculation considering errors on the PFU temperature of 1 °C and the IR calibration optimized for these measurements. This uncertainty will be displayed on some figures and removed for other for clarity. In any case the uncertainty on the measured emissivity remains much lower than the spatial distribution observed.

3.1. Emissivity pattern of the sectors Q4B and Q3B post-C4

A total of 30 PFUs have been measured with different PFU locations consecutive in the ripple modulation (20° period representing about 25 PFU) over two sectors. The set is composed of 14 ITER-grade PFUs and 16 W-coated graphite PFU divided into 2 components (located on the low and high field sides of the divertor). The emissivity maps obtained for these PFUs are shown in the figure 9 b) and d) superimposed to the pictures taken in the machine after the C4 campaign figure 9 a) and c). In addition to the exposed PFUs and for comparison, measurement have also been performed for unexposed ITER-grade and W-coated PFUs as shows in figure 10 b). The poloidal and toroidal distributions found on the W-coated PFUs (Q4B sector, figure 9 b) are consistent with the pattern found with in-situ measurement in the previous section (figure 3) with some differences on the high emissivity regions as discussed in the subsection 2.5.

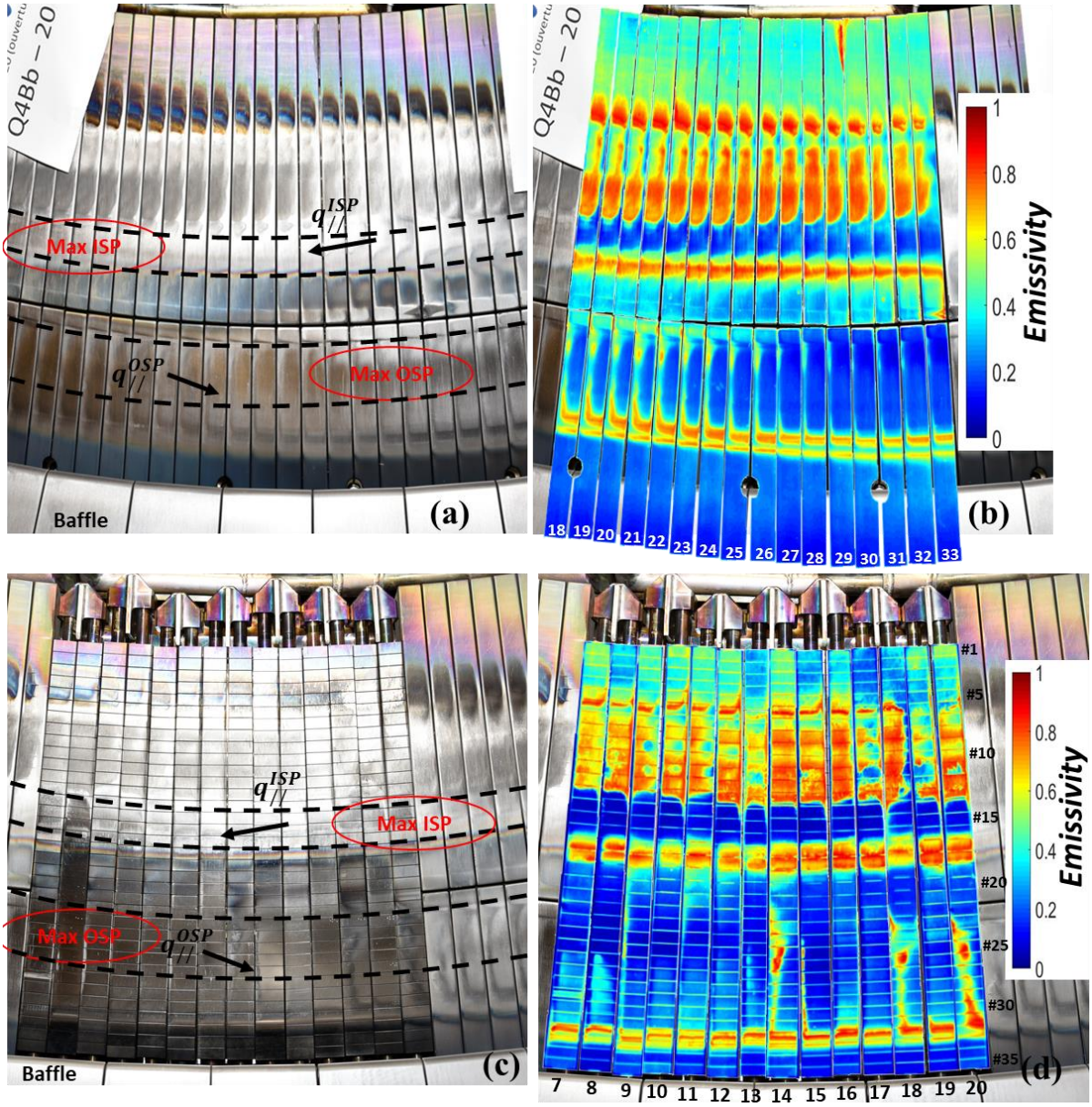

Figure 9. (a) Picture of the Q4B sector after the 2019 campaign (C4). Part of the divertor baffle can be seen at the bottom. (b) W-coated emissivity map from ex-situ measurement superimposed to the Q4B sector picture. (c) Picture of the Q3B sector after the 2019 campaign (C4). (d) ITER-like emissivity map from ex-situ measurement superimposed to the Q3B sector picture. The radial strike point extension are indicated with dotted lines in the pictures as well as the maximum heat load areas due to the ripple modulation in red.

On the OSP region of the W-coated PFU (figure 9 b) the emissivity is found minimal down to 0.08 slightly lower than non-exposed W-coated PFUs from 0.09 to 0.15 (figure 10 b). This lower emissivity is due to a decrease of the roughness in this area and a cleaning of the surface in comparison to non-exposed PFU which are slightly polluted by their manufacturing (see next section 3.2). Because of the 0.5 mm toroidal bevel, the emissivity is higher in the magnetically shadowed areas (left hand part of the PFU for the OSP) up to 0.7 for the OSP PFU #22, due to impurity redeposition from neutral particles near the leading edge as observed in [36]. The poloidal extension of the low emissivity area is about 10 cm. The toroidal extension of this area is coherent with the ripple modulation of the magnetic field: broader areas where the incident angle is minimal (<0.5°) around PFU#19 and thinner areas where the

outer incident angle is maximal (>2°) around PFU#32 (as illustrated in figure 12, the grey area are the magnetically shadowed area). The other area with high emissivity is at the transition, in the far SOL and poloidal direction, from the wetted area (top part) to the magnetic shadowed area due to the baffle (bottom part). This area exhibits emissivity up to 0.75 on the whole toroidal extension of the divertor. In the magnetic shadowed area under the baffle, the emissivity lies between 0.3 (close to the wetted area) and 0.15 (10 cm away under the baffle).

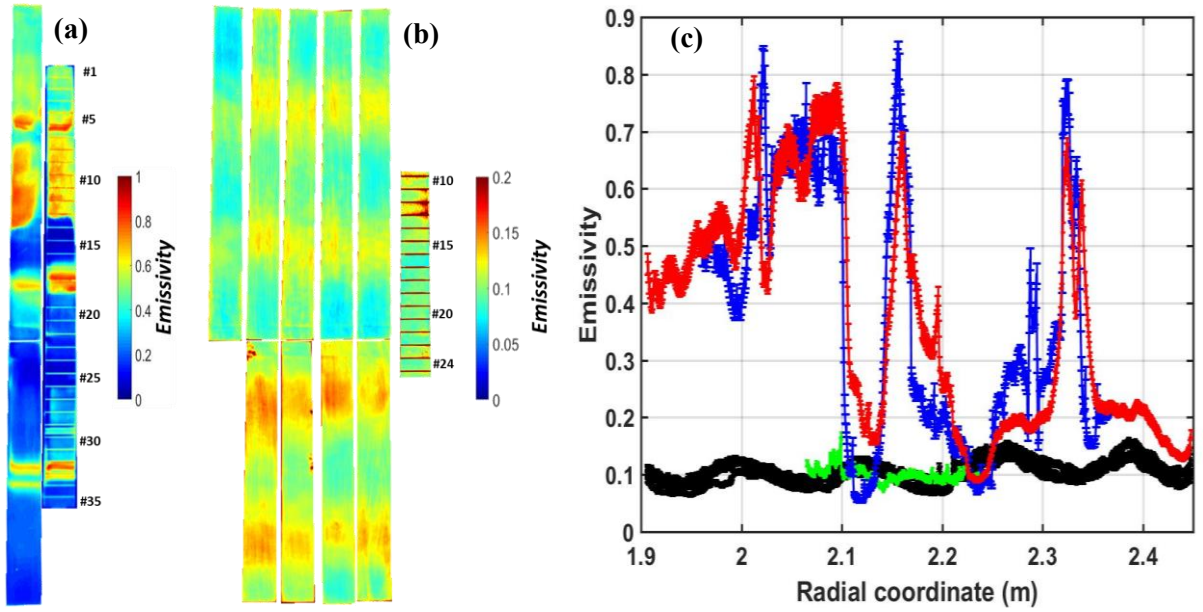

Figure 10. (a) Emissivity map after C4 for W-coated PFUs and ITER-like PFU from the location #7 of the sectors Q4B and Q3B, respectively (same location in the ripple pattern). (b) Emissivity map for non-exposed PFUs (9 W-coated PFUs and one ITER-grade PFU). (c) Emissivity distribution for (black) non-exposed W-coated PFUs, (green) non-exposed ITER-grade PFU, (red) W-coated after C4 and (blue) ITER-grade PFU after C4 extracted from figure (a).

On the ISP region of the W-coated PFU (figure 9 b) the emissivity is found minimal down to 0.12 in the range of the unexposed PFU and slightly higher than observed on the OSP area. A first difference is observed on the poloidal extension of this low emissivity (net erosion) area, lower than 3cm for the ISP area and 10cm for the OSP limited by the baffle shadowing. Another difference is observed in the toroidal direction, contrary to the OSP region, the emissivity is found uniform on the ISP even for the ISP PFU#32 where the incident angle is minimal about 0.4° inducing strong magnetic shadowing due to the 0.5 mm bevel. On the ISP, plasma temperature, particle and heat flux are found to be lower, therefore local erosion and redeposition might also be lower on the ISP than the OSP. At the border with the private flux region, just below the ISP area, iridescent appears and high emissivity up to 0.8 is observed with variation from 0.12 to 0.8 within a few cm. In the private flux region, the emissivity is about 0.4 until the gap between the inner and outer PFUs. On the scrape off layer side (top part in figure 9 b), the maximal emissivity is about 0.85 with sharp transition within a few mm from the net erosion area. The emissivity pattern exhibits also a non-uniform variation with bumps and hollows.

PFU#	7	8	9	10	11	12	13	14	15	16	17	18	19	20
h MB#15 ISP (mm)	-0,3	0,29	-0,06	0,27	-0,24	0,01	0,31	0,06	0,04	-0,37	0,67	-0,37	0,42	0,17
Average incident angle (°)	0,42	0,46	0,52	0,62	0,76	0,92	1,08	1,24	1,4	1,53	1,65	1,71	1,76	1,76
Toroidal shadowing (mm)	40,92	/	6,61	/	18,09	/	/	/	/	13,85	/	12,39	/	/
MB shadowing (%)	100,0	/	21,8	/	62,8	/	/	/	/	47,7	/	42,5	/	/
h MB#25 OSP (mm)	0,24	0,38	-0,31	-0,03	-0,22	0,22	0,25	-0,52	-0,11	0	0,28	-0,41	0,17	-0,57
Average incident angle (°)	2,28	2,24	2,15	2	1,83	1,61	1,38	1,15	0,92	0,72	0,56	0,45	0,38	0,36
Toroidal shadowing (mm)	/	/	8,26	0,86	6,89	/	/	25,90	6,85	/	/	52,20	/	90,72
MB shadowing (%)	/	/	27,7	1,3	22,8	/	/	90,7	22,7	/	/	100,0	/	100,0

Table 1. Misalignment (h) measured at the OSP (MB#25) and ISP (MB#15) of the WEST sector Q3B before the C4 experimental campaign. Positive values are prone to strong erosion on the leading edge, while negative values are prone to particle redeposition

A total of 14 unshaped ITER-grade PFUs have been measured after C4. Although no shaping, the overall pattern measured on the ITER-grade PFUs (see figure 9 d) is quite similar to the shaped W-coated PFUs. Once again, we found the low emissivity area at the strike point locations and sharp transition to high emissivity around these positions: in the outboard, in the baffle shadowing, in the private flux region and finally in the inboard, in the far scrape off layer area, few cm away from the inner strike point (see figure 10 a) and c)). However, the emissivity variation is higher with variation from 0.05 to 0.85 (factor 17) at a MB scale due to the complex plasma wall interaction because of the gap geometry, the various vertical misalignments and magnetic shadowing between PFUs As the ITER-grade PFUs are unshaped the knowledge of the PFU alignment is necessary to understand the emissivity pattern on the MB scale. To monitor the vertical misalignment (h) between adjacent PFUs, WEST is equipped with a 3D ball probe measuring arm which has a ± 18µm precision [35]. The misalignment measured for the 14 PFUs at the MB#15 and #25 locations (main strike point locations) have been summarized in the table 1, the toroidal shadowing induced by these misalignments are also shown with typical values of the incident angle at the different locations in the ripple modulation.

A complex pattern is observed especially in the outer area (see figure 11 a) featuring large toroidal variation in the plasma wetted area. For example (see figure 11.b), misaligned MBs (>0.2mm) exhibit a toroidal bump with emissivity of about 0.06 at the leading edge over the first 3 mm then a bump (up to 0.4 for PFU#7 (blue) and #8 (red), factor 7) about 5 mm away then slow decrease toward the trailing edge (down to 0.06 on PFU#8 (red) and PFU#17 (red) in figure 11 b)). This toroidal bump is observed on most of the PFU with overexposed leading edges and no shadowing from the upstream PFU (positive misalignment, see table 1) at the maximal loaded location for the PFU #07 and 08 and also close to the minimal loaded area with respect to the ripple modulation for the PFU#17. This pattern makes the IR analysis more complex as this pattern can evolve also during the campaign and with the strike point location [34]. The potential mechanisms leading to such feature, in particular the ion Larmor smoothing effect, have been studied in [34].

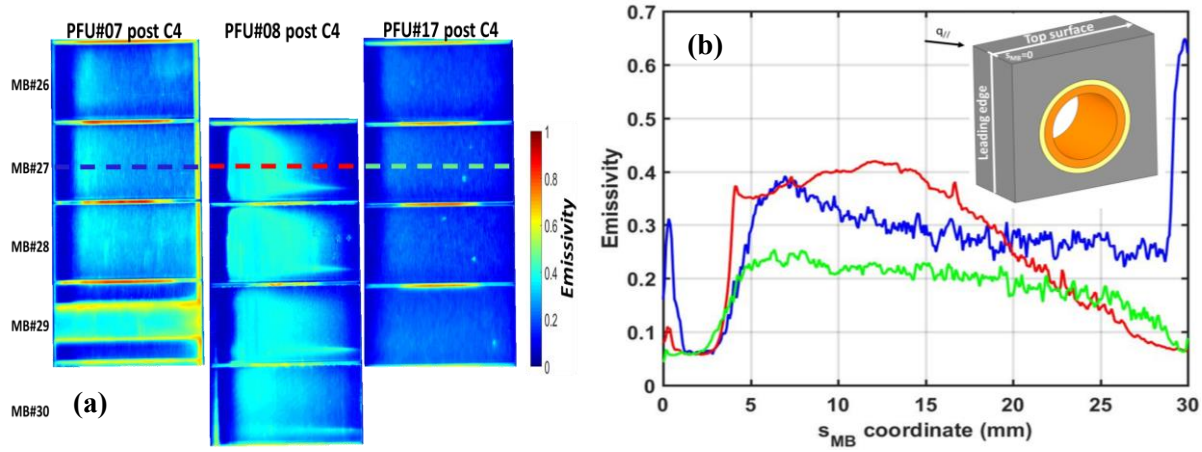

Figure 11. (a) Emissivity map of the PFU #07, #08 and #17 with a zoom in on the OSP area. (b) Emissivity along the curvilinear abscissa s_{MB} (toroidal direction) in the MB#27 center of the PFU (blue) #07, (red) #08 and (green) #17.

Still on the OSP area, the PFUs #14, #18 and #20 exhibit also strong emissivity up to 0.8 (figure 9.d) because of the recessed position of these PFU regarding the previous one (negative value of the misalignment, see table 1). The heat flux distribution and magnetic shadowing are computed with the PFCFlux code [21] on the sector Q3B for the pulse #55987 with the ITER-grade PFU moved with the measured misalignments, as displayed in figure 12 (magnetic shadowing is shown in grey color). The resulting simulations show strong shadowing due to upstream PFU for PFU#14, 18 and #20, which is consistent with the high emissivity observed for the outer MBs (thses MBs are prone to intensive particle redeposition). More surprisingly the emissivity at the ISP is always low for the 14 PFUs even for the PFU#7 where the emissivity at the ISP is down to 0.06 even though the whole ISP MB should be shadowed.

Campaign	PFU location													
C4	7	8	9	10	11	12	13	14	15	16	17	18	19	20
C3	20	12	9	10	11	8	13	14	15	16	/	/	19	7
C2	/	/	9	10	/	8	/	14	/	/	/	/	/	13
C1	/	/	9	10	/	/	/	14	/	/	/	/	/	13

Table 2. Location of the C4 PFU over the experimental campaigns.

The number of ITER-grade PFU increased over the campaigns and the PFU location have been also reshuffled between the different campaigns for the physics needs of the WEST scientific program, see table 2. However, no strong correlation appears between the emissivity pattern and the PFUs history, showing that the emissivity pattern is mainly the picture of the last campaign exposure.

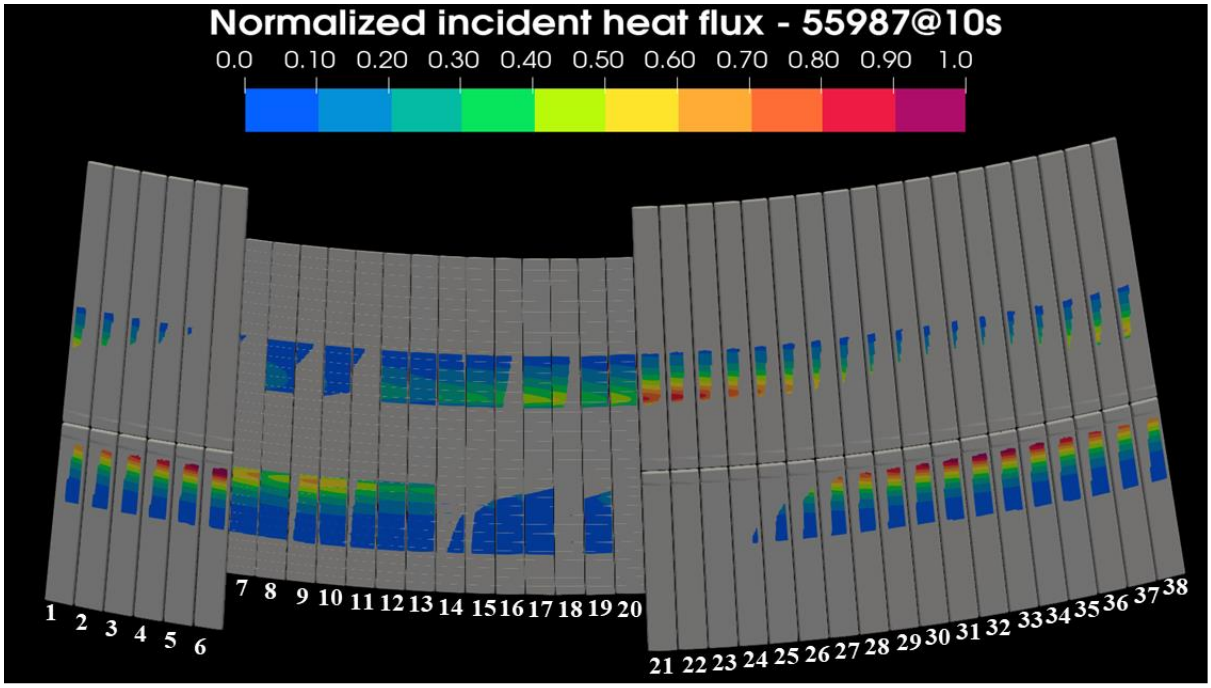

Figure 12. Normalized heat flux computed for the sector Q3B with the PFCFlux code [21] for the pulse #55987 without asymmetry and $\lambda_q = 6mm$ [26] projected to the divertor (no spreading factor in the private flux region). The ITER-grade PFU have been moved according to the measured misalignment. The white area corresponds to the magnetic shadowed area especially visible for the PFU 14, 18 and 20.

3.2. Comparison of post-mortem measurements and emissivity distribution

After C3 and C4 experimental campaigns, W-coated PFUs with additional W marker coating have been analyzed using ion beam analyses and scanning electron microscopy techniques [36]. The net erosion and deposition patterns in the inner and outer side of the WEST lower divertor were determined. As expected, strong erosion occurred at the inner and outer strike point area with an average net erosion rate of >0.1 nm/s over the campaigns. On the inner side, thick deposition composed of B, C, O and W of >10 µm for a 5-10 cm wide band is observed on the high field side with a sharp transition from the strong net erosion area. Outside this wide band moderate deposition is observed, even at the outer strike point location. These observations are in good agreement with the emissivity pattern observed with the in-situ (evolution during the campaign) and post-mortem measurements as illustrated in the figure 13.

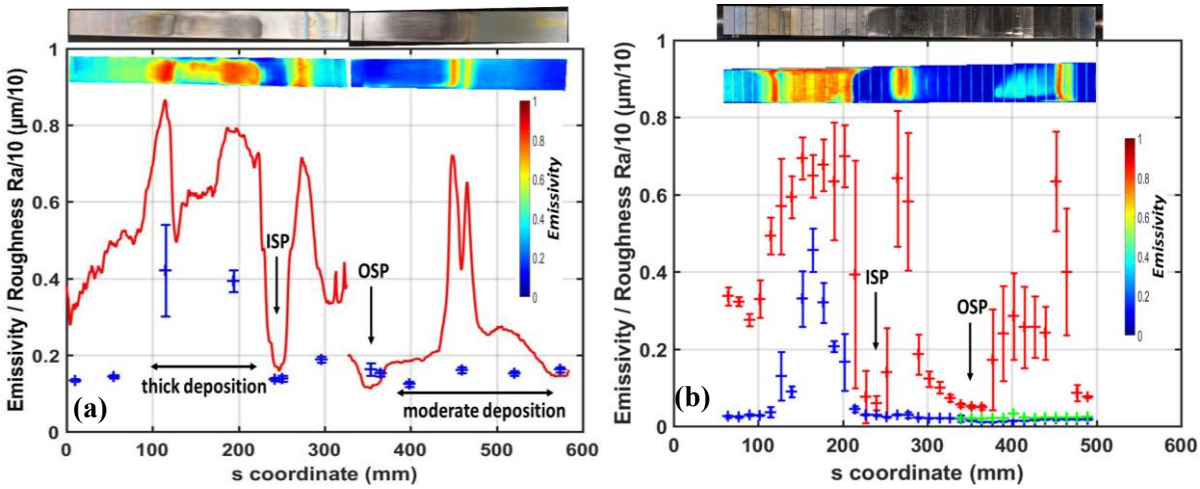

Figure 13. (a) Emissivity map and picture of the W-coated tiles ISP PFU#19 and OSP PFU#32 on the Q4B sector after C4. Comparison of the emissivity distribution (red), roughness measurements divided by 10 (blue) and the deposition observed in [36]. (b) Emissivity map and picture of the PFU #08 (ITER-grade) on the Q3B sector after C4. Comparison of the average emissivity with standard deviation (red) and roughness measurements divided by 10 for each MB (green) before and (blue) after WEST exposure see the roughness values in the table 3.

At both strike point location low emissivity about 0.1 close to the unexposed PFU (green crosses in figure 13 b) is found coherent with net erosion area. On the outer side, few cm away to the outer strike point (s≥350 mm), higher emissivity is found about 0.2 coherent with moderate deposition. On the inner side, the wide band of 5-10 cm observed on the C4 W-coated marker PFUs correspond to the high emissivity area up to 0.85 (for 100<s<220 mm).

In addition to emissivity measurements, roughness measurements have been performed at different location of the two PFUs at the inner and outer maximal loading location PFU#19 and #32, respectively see figure 13 a) and for the ITER-grade PFU#08 see figure 13 b). For the W-coated PFUs, the measured roughness is in the range from 1.3 to 1.8 µm, slightly lower than the unexposed PFUs measured at ~2.4 µm, except in the thick deposit area (from s~100 to ~220 mm in the figure 13) where the roughness increased up to ~4 µm with large standard deviation indicating non uniform roughness. This is coherent with strong deposition area and the subsequent surface modification observed with the in-situ emissivity measurement during the last 4 days of C4, experimental campaign performed with helium fueling (see figure 4 arrow #2). Equivalent pattern is observed for the ITER-grade PFU with roughness from 0.14 to 4.56 µm with low roughness in the strike point areas from 0.14 to 0.3 µm slightly lower to the values measured before installation and high roughness for the MB#6 to #12 up to 4.56 µm (see table 3). The standard deviation of the emissivity plotted in the figure 13 b) shows the strong emissivity variation at the MBs scale as for the MB#13 with emissivity from 0.05 to 0.85. Although, the high emissivities observed in the inner edge (s<100m), in the private flux region (s~280 mm) or in the outer side, in particular in the baffle shadowing area (s~450 mm), cannot be attributed to strong deposition or roughness increase. This could be explained by surface oxidation, as suggest the surface iridescence and post-mortem analysis that revealed the presence of W oxide in the deposit layer of ITER-grade PFU [37].

MB#	1	2	3	4	5	6	7	8	9
Emissivity	0.34 ± 0.02	0.32 ± 0.01	0.28 ± 0.02	0.33 ± 0.05	0.49 ± 0.05	0.57 ± 0.12	0.59 ± 0.05	0.69 ± 0.05	0.65 ± 0.05
Ra (µm) after WEST exposure	0.25 ± 0.03	0.25 ± 0.02	0.3 ± 0.02	0.28 ± 0.02	0.36 ± 0.13	1.3 ± 0.63	0.9 ± 0.15	3.3 ± 0.72	4.56 ± 0.56
Ra (µm) before WEST exposure									
MB#	10	11	12	13	14	15	16	17	18
Emissivity	0.68 ± 0.07	0.63 ± 0.15	0.7 ± 0.08	0.39 ± 0.29	0.08 ± 0.07	0.06 ± 0.02	0.14 ± 0.11	0.64 ± 0.18	0.58 ± 0.18
Ra (µm) after WEST exposure	3.2 ± 0.52	2.07 ± 0.14	1.66 ± 0.74	0.45 ± 0.08	0.3 ± 0.02	0.29 ± 0.02	0.23 ± 0.02	0.29 ± 0.02	0.29 ± 0.07
Ra (µm) before WEST exposure									
MB#	19	20	21	22	23	24	25	26	27
Emissivity	0.19 ± 0.05	0.12 ± 0.02	0.1 ± 0.01	0.07 ± 0.01	0.05 ± 0.01	0.05 ± 0.01	0.05 ± 0.01	0.17 ± 0.13	0.24 ± 0.12
Ra (µm) after WEST exposure	0.22 ± 0.02	0.21 ± 0.01	0.21 ± 0.01	0.21 ± 0.01	0.19 ± 0.09	0.14 ± 0.01	0.11 ± 0.01	0.11 ± 0.01	0.12 ± 0.01
Ra (µm) before WEST exposure					0.2	0.2	0.2	0.2	0.2
MB#	28	29	30	31	32	33	34	35	
Emissivity	0.28 ± 0.11	0.26 ± 0.1	0.26 ± 0.08	0.24 ± 0.07	0.63 ± 0.13	0.4 ± 0.16	0.09 ± 0.02	0.08 ± 0.01	
Ra (µm) after WEST exposure	0.14 ± 0.01	0.14 ± 0.01	0.16 ± 0.01	0.18 ± 0.01	0.19 ± 0.04	0.18 ± 0.01	0.18 ± 0.02	0.18 ± 0.01	
Ra (µm) before WEST exposure	0.32	0.22	0.21	0.22	0.22	0.23	0.22	0.23	

Table 3. Averaged emissivity and roughness measured on the ITER-grade PFU#08 of the sector Q3B after the C4 campaign.

3.3. Emissivity pattern in the inter-PFU gaps

After the C4 campaign, one of the actively cooled ITER-like PFU has been moved from minimum heat load area (PFU#18) to maximum heat flux area (PFU#8) on the OSP (see figure 12), in order to melt the monoblock #28 during the next experimental campaign (C5) [30]. This PFU has been exposed only to the C4 campaign (small heat loading and moderate erosion condition), with deuterium and helium plasmas, and C5 campaign with only deuterium plasma (high heat loading and intense erosion condition in the OSP). Figure 14 shows the emissivity measured for this PFU after each campaign and the cumulated energy conducted on the PFU with a spatial resolution corresponding to the MB size. After C5 the emissivity pattern has changed mainly into two areas, on the outer side from MB#23 to #30 corresponding to the plasma wetted area and on the inner side from MB#6 to #13 corresponding to the thick deposit area described in the previous section.

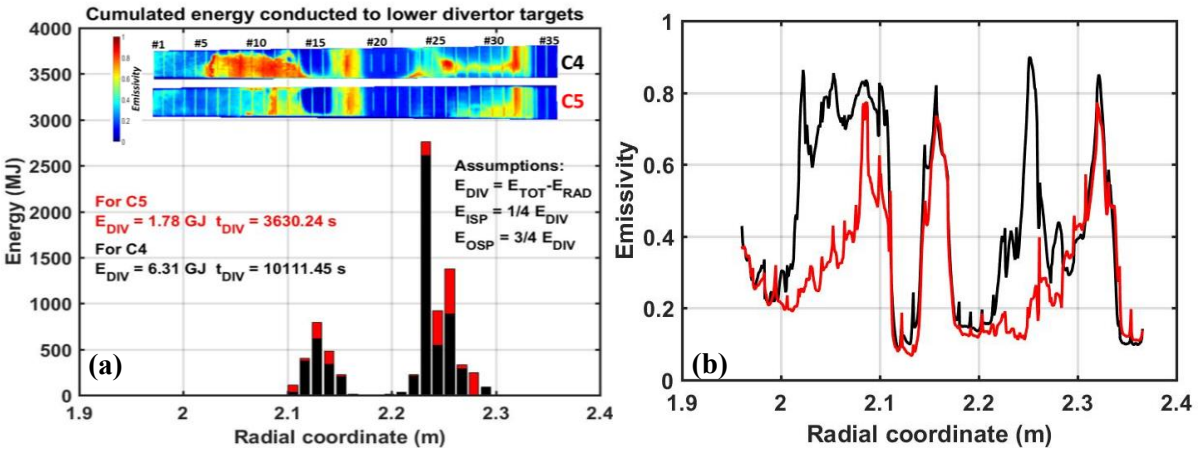

Figure 14. (a) Emissivity map for the same PFU from the sector Q3B after C4 and C5 located at the location #18 and #8, respectively. Illustration of the conducted energy to the lower divertor at the strike point location with asymmetry of 1/4 ISP and 3/4 OSP as observed in [26] and no consideration of decay length (λ_q). (black) Conducted energy during C4 and (red) C5. (b) Emissivity distribution along the same PFU from the sector Q3B after C4 (black) and C5 (red) located at the location #18 and #8, respectively.

For the inner side the emissivity decreased drastically after C5 especially for the MB#6 to #10 with emissivity 2 times up to 4 times lower than the post C4 measurements. This important reduction could come from a modification of the deposit observed in this region, further analyses are planned to characterize this area in terms of roughness, surface composition and deposit thickness with comparison to the post C4 PFUs not exposed to the C5 campaign. In the ISP area for the MB#14 to #16 the emissivity slightly decreases from ~0.1 post C4 to ~0.07 post C5. Finally, far away at the high field side of the PFU (R<2 m) and at the private flux region transition (R~2.15 m) the emissivity remains mainly unchanged.

Figure 15 shows the emissivity measurement with a zoom in on the OSP area from MB#23 to #30 with a spatial resolution of 0.08 mm/pixel. The emissivity strongly changed during C5 with an overall decrease from ~0.9 to ~0.1 because of the increase of the particle and heat loads.

- On MB#24, the emissivity decrease allows the visualisation of the 4 IR markers holes (prone to material redeposition).
- On MB#25, corresponding to the main OSP location during the last part of C5, exhibits low emissivity on the whole MB surface coherent with net erosion area.
- For the MB#26 to #30, the emissivity decreased in the MB center and increased at the leading edge, bottom part of the MB, during C5 despite the misalignment of +0.3 mm showing impurity deposition few cm away from the strike point location even with leading edge.

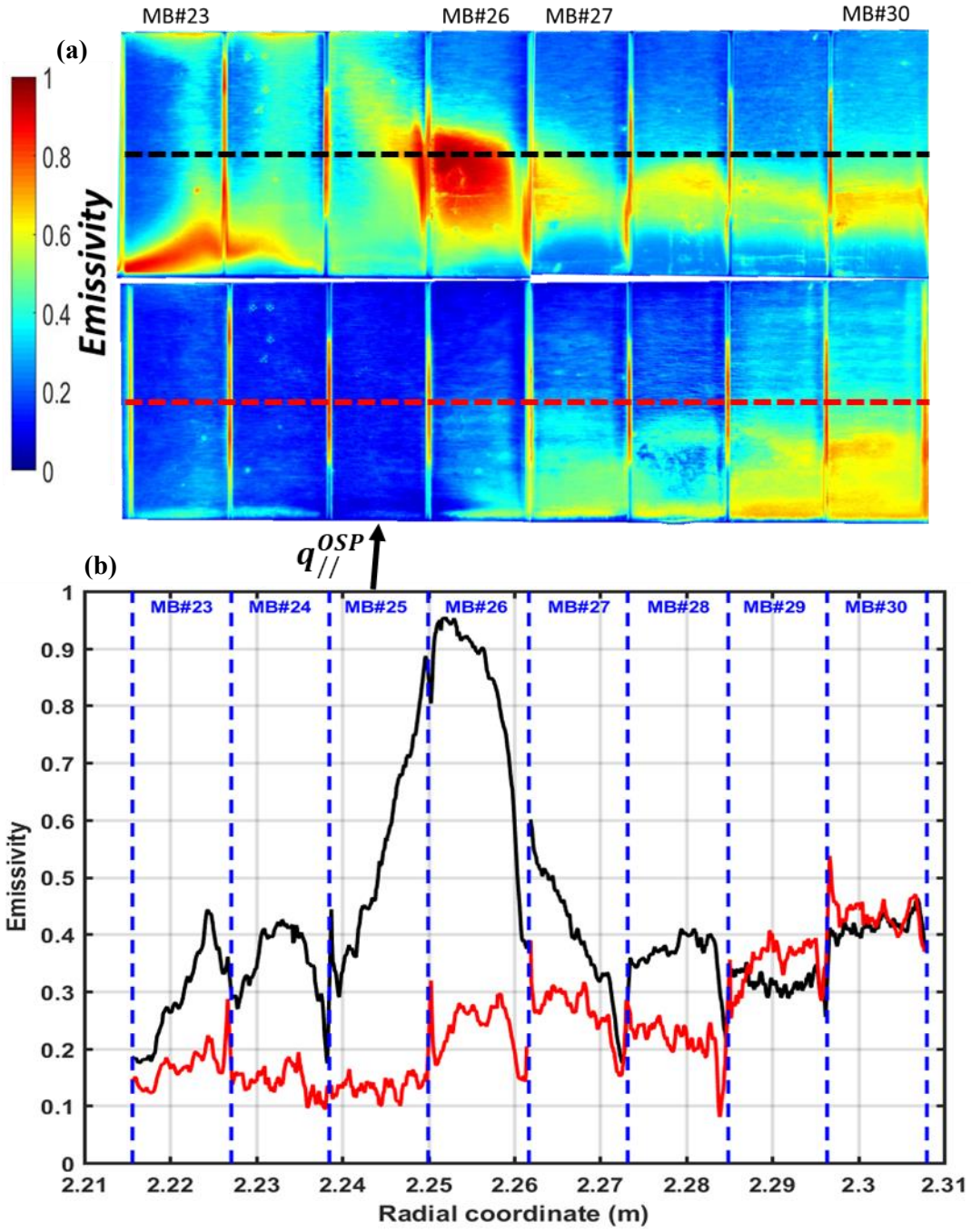

Figure 15. (a) Emissivity map (zoom in on the OSP area) for the same PFU from the Q3B sector after C4 (top) and C5 (bottom) located at the location #18 (lower heat loading) and #8 (higher heat loading), respectively. (b) Emissivity distribution after C4 (black) and C5 (red) in the middle of the PFU (dotted lines in (a)).

Figure 16 shows the emissivity of the top and lateral surfaces of the PFU#8 after C5 for the full PFU and zoom in at both strike point areas. On the PFU sides, on both leading and trailing edges, the measurement shows low and high emissivity on the wetted (because of the 0.3mm vertical misalignment [ref alex]) and shadowed areas respectively. The high emissivity area suggests impurity deposition in the inter-PFU gap of 0.5 mm. This impurity deposition occurs from the MB#5 to #18 on the high field

side and from MB#22 to #32 on the low field side corresponding to a poloidal extension higher than the strike point locations. Figure 17 shows the emissivity along the curvilinear abscissa for the MB at both strike point locations with identification of the leading and trailing edge. The measurement exhibits high emissivity ~0.8 up to 5 mm below the top surface for the outer leading edge and up to 0.4 for the outer trailing edge. For the inner side the emissivity is in the range of 0.6 on both edges with also 5mm depth in the gap. This depth corresponds to 10 times the gap size of 0.5 mm between two PFUs. Below this area, the emissivity decreases down to ~0.1 which indicates the limit of the plasma impact. On the OSP leading edge of the MB#28, we can distinguish a rectangle (2.3 mm depth and 9 mm width) corresponding to the surface in front of the PFU#7 groove where the W melting occurs [30]. This area exhibits high emissivity even at the melting location probably due to deposition occurring during the month of operation after the melting experiment with the OSP away from the MB#28.

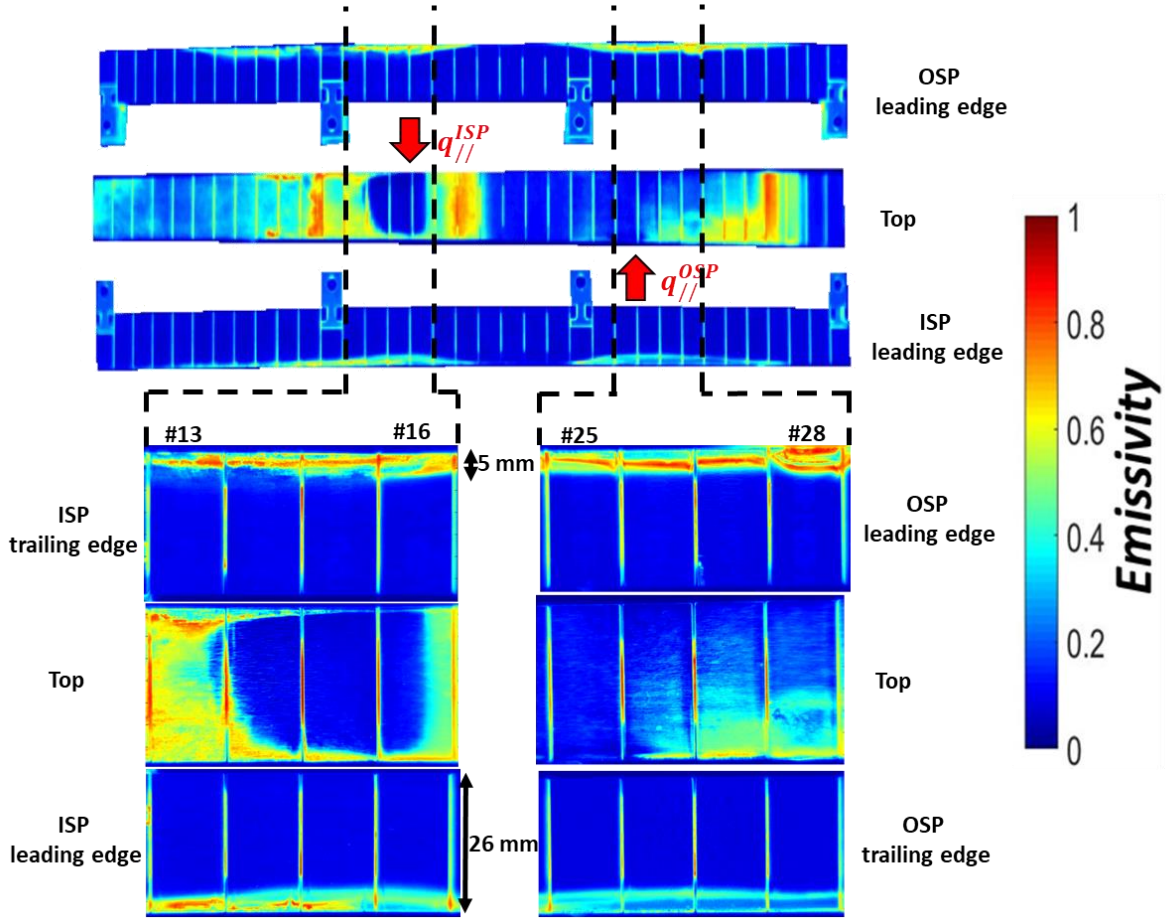

Figure 16. Emissivity map of the PFU #8 after C5. (top) Full PFU with top and lateral sides with the 25 mm lens (0.7mm/pixel). (bottom) Zoom in for 4 MBs at the inner (left) and outer (right) strike point locations with the 50 mm lens (0.08mm/pixel).

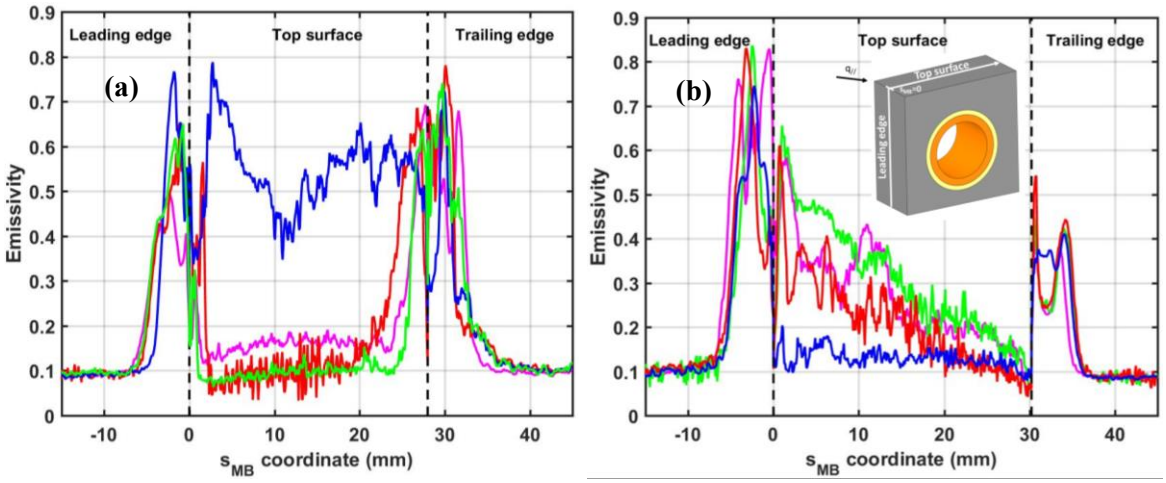

Figure 17. Emissivity of PFU #8 after C5 measured in the MB center along the curvilinear abscissa s_{MB} with s_{MB} =0 mm at the junction between the leading edge and the top surface. (a) Inner strike point MB (blue) #13, (red) #14, (green) #15 and (magenta) #16. (b) Outer strike point MB (blue) #25, (red) #26, (green) #27 and (magenta) #28.

4. Conclusion

This paper summarizes the emissivity measurements performed on the plasma facing components of the WEST lower divertor inside the machine during the C4 (2019) experimental campaign for the W-coated graphite PFUs and in laboratory after removing the W-coated and ITER-grade PFUs. The measurements clearly show a complex pattern with strong emissivity variation and his evolution during the campaign.

In the machine, the emissivity monitoring along the C4 campaign has been performed with the emissivity estimation for 160 pairs of pulses along the campaign. This monitoring has shown strong correlation of the emissivity distribution to the plasma operation, especially for the strike point location, plasma species and plasma current. On the inner side, emissivity increases from 0.12 to 0.65 has been observed 15 cm away from the strike point location. As well as fast modification of the emissivity distribution during the last 4 days with an emissivity decrease from 0.6 to 0.4 few cm away from the strike point location. During these days helium plasmas at I_p=300kA have been performed after a campaign with mainly deuterium plasmas at 500kA (with B_T=3.7T). On the outer side the monitoring has shown that the emissivity distribution strongly depends to the strike point location with variation from 0.12 to 0.2 in the wetted area. When the strike point is moved at a new location the emissivity starts to decrease down to 0.12 locally (where Te>20 eV) and increase at the previous strike point location up to 0.2. These emissivity modifications occur in few pulses with additional LH heating of about 4 MW and cumulated conducted energy of few hundred of MJ. Finally, the emissivity monitoring has not shown strong modification of the emissivity due to the wall conditioning by deuterium or helium GDC or even boronization with equivalent emissivity distribution observed before and after three pulses after wall conditioning performed.

Post-mortem measurements have been also performed with dedicated laboratory testbeds. These measurements confirmed the in-situ observations in terms of complex spatial distribution and sharp spatial evolution of the emissivity from 0.05 to 0.85 at a MB scale. These measurements have shown emissivity variation over a ripple modulation with the measurement of 16 W-coated graphite PFUs and 14 ITER-grade PFUs. The emissivity pattern is coherent with the ripple modulation and the modulation of the shadowed area due to upstream PFU with high emissivity in the shadowed area. The ITER-grade

PFUs have shown equivalent pattern to the W-coated PFUs with more complex distribution in the strike point area with strong toroidal variation from 0.06 to 0.4 in few mm in the toroidal direction. The comparison of the emissivity distribution with roughness measurements indicate that the high emissivity could be attributed to different causes. In the thick deposit area (mainly B, C, O and W [36]) the roughness is in the range of the IR wavelength leading to an increase of the emissivity in addition to the compound of the deposit which are also a good emitter as B and C. The other areas with high emissivity could be due to oxide as the iridescent color suggest as well as first Raman measurements.

The number of ITER-grade PFU increased over the campaigns and the PFU location have been also reshuffled between the different campaigns for the physics needs of the WEST scientific program. However, no strong correlation appears between the emissivity pattern and the PFUs history showing that the emissivity pattern is mainly the picture of the last campaign exposure. This point combined to the strong emissivity variation (factor 17) with complex pattern with strong variation in the poloidal and toroidal directions imply the necessity to develop an in-situ procedure to measure the emissivity at a day scale to be able to derive accurate surface temperature from IR measurement over all the experimental campaigns

Acknowledgments

This work has been carried out within the framework of the EUROfusion Consortium and has received funding from the Euratom research and training programme 2014–2018 and 2019-2020 under grant agreement No 633053. The views and opinions expressed herein do not necessarily reflect those of the European Commission and ITER Organization.

References

[1] M. Houry et al., "The very high spatial resolution infrared thermography on ITER-like tungsten monoblocks in WEST Tokamak", Fusion Engineering and Design 146 (2019) 1104–1107. https://doi.org/10.1016/j.fusengdes.2019.02.017

[2] B. Sieglin et al., "Power load studies in JET and ASDEX-Upgrade with full-W divertors", Plasma Phys. Control. Fusion 55 (2013) 124039. https://doi.org/10.1088/0741-3335/55/12/124039

[3] B. Sieglin et al., "Real-Time Infrared Thermography at ASDEX Upgrade", Fusion Science and Technology 69 (2016) 580–585. https://doi.org/10.13182/FST15-183

[4] X. Courtois et al., "Full coverage infrared thermography diagnostic for WEST machine protection", Fusion Engineering and Design 146 (2019) 2015–2020. https://doi.org/10.1016/j.fusengdes.2019.03.090

[5] I. Balboa et al., "Upgrade of the infrared camera diagnostics for the JET ITER-like wall divertor", Review of Scientific Instruments, 83 (2012) 10D530. https://doi.org/10.1063/1.4740523

[6] G. Arnoux et al., "A protection system for the JET ITER-like wall based on imaging diagnostics", review of scientific instruments, 83 (2012) 10D727. https://doi.org/10.1063/1.4738742

[7] M. Jakubowski et al., "Infrared imaging systems for wall protection in the W7-X stellarator", Review of Scientific Instruments, 89 (2018) 10E116. https://doi.org/10.1063/1.5038634

[8] T. Hirai et al., "Use of tungsten material for the ITER divertor", Nuclear Materials and Energy 9 (2016) 616-622. https://doi.org/10.1016/j.nme.2016.07.003

[9] R.A. Pitts et al., "Physics conclusions in support of ITER W divertor monoblock shaping", Nuclear Materials and Energy 12 (2017) 60-74. https://doi.org/10.1016/j.nme.2017.03.005

[10] J.L. Terry et al., "Divertor IR thermography on Alcator C-Mod", Rev. Sci. Instrum. 81, 10E513 (2010) https://doi.org/10.1063/1.3478669

[11] N. Fedorczak et al., "Infra-red thermography estimate of deposited heat load dynamics on the lower tungsten divertor of WEST", Physica Scripta T171 (2020). https://doi.org/10.1088/1402-4896/ab4e3d

[12] P. Vondracek et al., "Divertor infrared thermography on COMPASS", Fusion Engineering and Design 146 (2019) 1003-1006. https://doi.org/10.1016/j.fusengdes.2019.01.142

[13] R.P. Doerner et al., “Investigation of He–W interactions using DiMES on DIII-D”, Physica Scripta T167 (2016) 014054. https://doi-org.lama.univ-amu.fr/10.1088/0031-8949/T167/1/014054
[14] J. Gaspar et al., “Emissivity measurement of tungsten plasma facing components of the WEST tokamak”, Fusion Engineering and Design 149 (2019) 111328. https://doi.org/10.1016/j.fusengdes.2019.111328
[15] T.K. Gray et al., “Dependence of divertor heat flux widths on heating power, flux expansion, and plasma current in the NSTX”, Journal of Nuclear Materials 415 (2011) S360–S364. https://doi.org/10.1016/j.jnucmat.2011.01.029
[16] M. Diez et al., “In situ observation of tungsten plasma-facing components after the first phase of operation of the WEST tokamak”, Nuclear Fusion 61,10, (2021), 106011. https://doi.org/10.1088/1741-4326/ac1dc6
[17] A. Puig Sitjes et al “Wendelstein 7-X Near Real-Time Image Diagnostic System for Plasma-Facing Components Protection”, Fusion Science and Technology 74 (2018) 116-124. https://doi.org/10.1080/15361055.2017.1396860
[18] J. Gaspar et al., “In-situ assessment of the emissivity of tungsten plasma facing components of the WEST tokamak”, Nuclear Materials and Energy, 25 (2020) 100851. https://doi.org/10.1016/j.nme.2020.100851
[19] J. Bucalossi et al., “Operating a full tungsten actively cooled tokamak: overview of WEST first phase of operation”, Nuclear Fusion https://doi.org/10.1088/1741-4326/ac2525
[20] M. Missirlian et al., “The WEST project: Current status of the ITER-like tungsten divertor”, Fusion Engineering and Design 89 (2014) 1048-53. https://doi.org/10.1016/j.fusengdes.2014.01.050
[21] M. Firdaouss et al., “Heat flux depositions on the WEST divertor and first wall components”, Fusion Engineering and Design 98-99 (2015) 1294-8. https://doi.org/10.1016/j.fusengdes.2014.12.024
[22] J. Gaspar et al. “First heat flux estimation in the lower divertor of WEST with embedded thermal measurements”, Fusion Engineering and Design 146 (2019) 757-760. https://doi.org/10.1016/j.fusengdes.2019.01.074
[23] Y. Corre et al., “Integration of fiber Bragg grating temperature sensors in plasma facing components of the WEST tokamak”, Review of Scientific Instruments, 89 (2018) 063508. https://doi.org/10.1063/1.5024514
[24] R. Dejarnac et al, Flush-mounted Langmuir probes in the WEST tokamak divertor, Fusion Engineering and Design 163 (2021) 112120. https://doi.org/10.1016/j.fusengdes.2020.112120
[25] M.H. Aumeunier et al., “Infrared Thermography in Metallic Environments of WEST and ASDEX Upgrade”, Nuclear Materials and Energy 26 (2021) 100879. https://doi.org/10.1016/j.nme.2020.100879
[26] J. Gaspar et al. “Divertor power loads and scrape off layer width in the large aspect ratio full tungsten tokamak WEST”, Nuclear Fusion 61 (2021) 096027. https://doi.org/10.1088/1741-4326/ac1803
[27] J. Blum et al., “Reconstruction of the equilibrium of the plasma in a Tokamak and identification of the current density profile in real time”, Journal of Computational Physics 231 (2012) 960-980. https://doi.org/10.1016/j.jcp.2011.04.005
[28] A. Grosjean et al., “First analysis of the misaligned leading edges of ITER-like plasma facing units using a very high resolution infrared camera in WEST”, Nuclear Fusion 60 (2020) 106020. https://doi.org/10.1088/1741-4326/ab9fa6
[29] M. Richou et al., predamaged paper submitted
[30] Y. Corre et al., “Sustained W-melting experiments on actively cooled ITER-like Plasma Facing Unit in WEST”, Physica scripta 96 (12) (2021) 124057 https://doi.org/10.1088/1402-4896/ac326a
[31] E. Tsitrone et al. “Investigation of plasma wall interactions between tungsten plasma facing

components and helium plasmas in the WEST tokamak", Nuclear Fusion https://doi.org/10.1088/1741-4326/ac2ef3

[32] J. Bucalossi et al., "The conditioning procedures in Tore Supra after CIEL implementation", Journal of Nuclear Materials 313–316 (2003) 263–268. https://doi.org/10.1016/S0022-3115(02)01339-9

[33] C. Talatizi et al. "Inverse radiation problem with infrared images to monitor plasma-facing components temperature in metallic fusion devices" Fusion Engineering and Design 159 (2020) 111867 https://doi.org/10.1016/j.fusengdes.2020.111867

[34] A. Grosjean et al., "Interpretation of temperature distribution observed on W-ITER-like PFUs in WEST monitored with a very-high-resolution IR system", Fusion Engineering and Design 168 (2021) 112387. https://doi.org/10.1016/j.fusengdes.2021.112387

[35] J.P. Gunn et al., "Thermal loads in gaps between ITER divertor monoblocks: First lessons learnt from WEST", Nuclear Materials and Energy 27 (2021) 100920. https://doi.org/10.1016/j.nme.2021.100920

[36] M. Balden et al., "Erosion and redeposition patterns on entire erosion marker tiles after exposure in the first operation phase of WEST", Physica Scripta 96 (2021) 124020. https://doi.org/10.1088/1402-4896/ac2182

[37] C. Martin et al., "First post-mortem analysis of deposits collected on ITER-like components in WEST after the C3 and C4 campaigns", Pysica Scripta 96 (2021) 124035. https://doi.org/10.1088/1402-4896/ac267e